CrystEngComm

PAPER

View Article Online
View Journal

Cite this: DOI: 10.1039/c5ce00173k

Structural and optical characterization of ball-milled copper-doped bismuth vanadium oxide ($BiVO_4$)†

Victor-Ishrayelu Merupo,[ab] Subramaniam Velumani,*[a] Karolina Ordon,[bc] Nicolas Errien,[b] Jacek Szade[d] and Abdel-Hadi Kassiba*[b]

Received 25th January 2015,
Accepted 23rd March 2015

DOI: 10.1039/c5ce00173k

www.rsc.org/crystengcomm

Copper-doped $BiVO_4$ nanoparticles were synthesized by a mechano-chemical method under optimized conditions to obtain a monoclinic scheelite structure. The crystal structure and its evolution with doping were investigated by X-ray powder diffraction, micro-Raman spectroscopy, field emission scanning electron microscopy (FE-SEM) and high-resolution transmission electron microscopy (HRTEM). Spherical shape particles with sizes ranging between 40 and 160 nm, which possess a monoclinic scheelite structure, were obtained. From the structural data analysis, it can be observed that the particle size decreases and distortions occur as the copper content increases in doped $BiVO_4$. Chemical bonding and valence states of the Bi-4f, V-2p, O-1s and Cu-2p ions were investigated by XPS which revealed the location of Cu ions in the host lattice of $BiVO_4$ in agreement with EPR investigations. UV-visible absorption experiments showed a broad band in the visible range with a small shift of the energy band-gap from 2.41 eV for undoped $BiVO_4$ to 2.34 eV for 10 at.% Cu–$BiVO_4$. Additional absorption band shoulders and widening of the optical absorption spectrum in the visible range with a well crystalline monoclinic scheelite structure pave the way for efficient visible light-driven photocatalytic activity. Photocatalytic measurements reprinted in supplementary data.

Due to environmental requirements for the preservation of water and the Earth's atmosphere, new photocatalytic materials have become the subject of intensive research during the past decade.[1] Particularly, devices using functional semiconducting oxides is a matter of interest in the search for an alternative renewable, clean and sustainable energy.[2] The environmental or energy applications of such materials are purely based on photocatalytic reactions catalyzed by the solar spectrum. The efficiency of these photocatalysts depends on their ability to absorb a large fraction of solar spectrum including the visible part. Several classes of materials were then developed for various applications. They are exploited in hydrogen production by water dissociation or for environmental protection for water and atmosphere depollution by degradation of pollutants generated by industrial or human activities. In this context, the most popular photocatalyst used so far is titanium dioxide (TiO_2) which was the subject of an impressive number of reports during the last two decades. Although it possesses a large band gap (3.2 eV), TiO_2 as a photocatalyst has shown a high efficiency only in the UV spectral range, *i.e.* 4–6% of the solar irradiation spectrum.[3]

The search for alternative functional semiconducting oxides was motivated by the need to develop visible light active systems based on bismuth vanadate ($BiVO_4$) as reported recently by our group[4] and also its well-known ferroelasticity and ionic conductivity.[5] It has been previously shown that $BiVO_4$ is a potential candidate in several solar radiation-driven applications including water splitting for hydrogen production and degradation of organic pollutants.[6] These performances are also associated with low cost and high stability in aqueous media as a visible light-driven photocatalyst.[7] However, the photocatalytic reactions are highly dependent on the structural polytypes of the material which influence the electronic and optical behaviours. $BiVO_4$ crystallizes in three different forms, *viz.*, monoclinic scheelite, tetragonal scheelite and tetragonal zircon. According to previous reports, photocatalytic activity of the monoclinic phase $BiVO_4$ shows better efficiency than those of the

[a] Department of Electrical Engineering (SEES), CINVESTAV-IPN, Zacatenco, Av IPN #2508, Col Zacatenco, D.F., C.P. 07360, Mexico. E-mail: velu@cinvestav.mx; Fax: +52 5557474003; Tel: +52 5557474001
[b] Institute of Molecules & Materials of Le Mans (IMMM) UMR CNRS, Universite du Maine, Le Mans 72085, France. E-mail: kassiba@univ-lemans.fr; Fax: +33 (0)243833518; Tel: +33 (0)243833512
[c] Institute of Physics, Jan Dlugosz University in Czestochowa, 13/15 Al. Armii Krajowej, Czestochowa 42 200, Poland
[d] A. Chełkowski Institute of Physics and Silesian Centre of Education and Interdisciplinary Research, University of Silesia, Ul. Uniwersytecka 4, Katowice 40-007, Poland

† Electronic supplementary information (ESI) available. See DOI: 10.1039/c5ce00173k

tetragonal zircon and tetragonal scheelite structures.[8] From theoretical and numerical calculations based on DFT, it is found that the effective hybridization of the Bi 6s state and O 2p state as the upper valence band (HOMO) with V 3d states as the lower conduction band (LUMO) would be responsible for the low bandgap of 2.4 eV in the $BiVO_4$ monoclinic scheelite structure.[9]

Despite stabilizing the monoclinic scheelite phase with different morphologies as nanosized objects (nanoparticles, nanorods, nanowires, *etc.*), pure $BiVO_4$ shows relatively low photocatalytic efficiency under visible light.[10] The problem of electron–hole pair photogeneration in the visible range with short life-times and high rates of charge carrier recombination requires improvement by relevant approaches to overcome such limitations. Recently, Yao *et al.* has reported that the mesoporous structure of $BiVO_4$ represents a good option to overcome these shortcomings.[11] However, the strategy of doping $BiVO_4$ structure by suitable metallic elements such as transition metal ions is expected to optimize the electronic features required for photocatalysis. Thus, substitutional doping of $BiVO_4$ with defined rates up to 10 at.% with a stable monoclinic structure is a challenging task with the aim to fine-tune the optical and chemical properties.[12] Previously, Xu *et al.* synthesized Fe, Co and Cu-loaded $BiVO_4$ by wet impregnation method and found that the Cu-loaded $BiVO_4$ has shown the highest photocatalytic activity amongst all other transition metals.[13] So far, doped $BiVO_4$ was synthesized by several methods such as sol–gel,[11] hydrothermal,[13] impregnation method,[14] solution combustion,[15] solid-state reaction,[16] co-precipitation[17] and metal–organic decomposition.[18] Venkatesan *et al.* reported that the high energy ball milling technique is one of the simple and effective pathways to achieve highly monoclinic $BiVO_4$ particles with an average crystalline domain size of 20 nm and an energy band gap (E_g) of 2.36 eV.[4]

The present work is dedicated to ball-milled $BiVO_4$ with Cu-doping. The optimized synthesis parameters such as ball per powder (BPR) ratio and rotation speed of synthesis chamber per min (rpm) were defined from our previous reports.[4] Post-synthesis treatments were performed to improve the structural features such as pure crystalline phase and substitution of Cu ions inside the crystal sites of $BiVO_4$. To achieve such tasks, characterization techniques including micro-Raman and X-ray powder diffraction (XRD) for structural studies and field emission scanning electron microscopy (FE-SEM) and high-resolution transmission microscopy (HR-TEM) for morphology, particle size and homogeneity of the chemical materials were used. These studies were also supported by X-ray photoelectron spectroscopy (XPS) which probes the involved chemical bonding. As Cu^{2+} ions are paramagnetic, electron paramagnetic spectroscopy (EPR) was performed on several doped samples to evaluate the degree of substitution and to inform about the distribution of doped copper inside the synthesized materials. The evolution of the optical band gap was investigated and correlated with the structural and electronic changes induced by Cu doping.

Experimental details

Synthesis

The high energy ball milling (HEM) technique is a suitable process for producing large-scale, micro- and nanosized materials for several applications. The HEM synthesis is based on a strong mechanical energy transfer created by colliding hard phase materials like carbides or ceramics with reactants such as metals, alloys, and optimized composites. During the HEM process, repeated fracturing and welding ensures that the milling operations will lead to the solid-state reaction of the individual materials resulting in the formation of the final composite materials. By this means, doping or alloying chemical elements can form micro- or nanostructured powders with defined stoichiometry and crystalline order. Fig. 1 illustrates the main steps involved in the HEM synthesis.

For the synthesis of Cu-doped $BiVO_4$ powders, the starting materials are bismuth oxide (Bi_2O_3, Sigma Aldrich, 99.99%), vanadium oxide (V_2O_5, Sigma Aldrich, 99.97%) and metallic copper grains (Sigma Aldrich, <1 mm, 99.9%). The reactants were used at different atomic percentages (x = 1, 5 and 10%) in a stoichiometric ratio of $[1:(1-x):x]$ and blended homogenously by using an agate mortar to obtain a total mixture weight of 7.7 grams, which is equal to the weight of one tungsten carbide (WC) ball, and loaded into an 80 ml WC made jar with balls of 9 mm diameter. A Retsch-planetary high

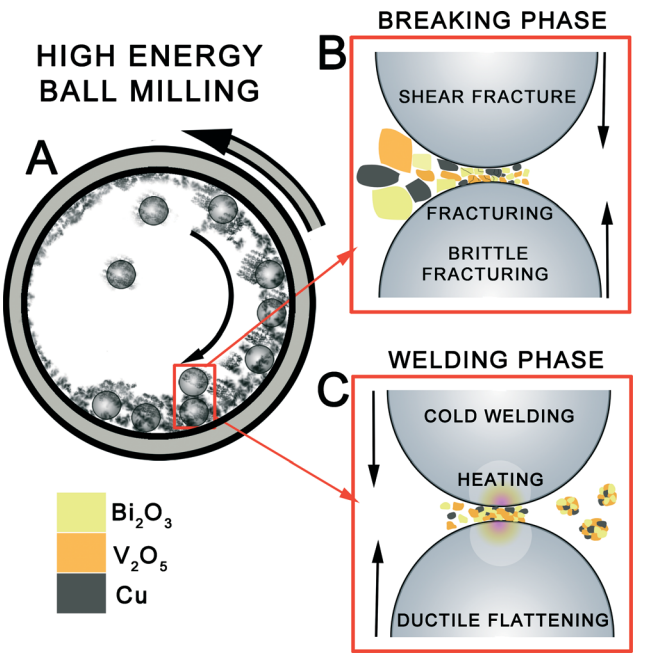

Fig. 1 Schematic representation of the high energy ball milling synthesis mechanism for Cu-doped $BiVO_4$ nanoparticles: (A) The content of the rotating (rpm) reaction chamber with hard balls and a mixture of the initial reactants at defined stoichiometric ratios which define the final product. (B) The breaking phase, where repeated fracturing of bulk reactants causes formation of composite particles with desired compositions. (C) The welding phase, where small agglomeration of particles forms the final morphology of the powder.

energy ball mill PM 400 was used, and the milling was performed for 6 hours at 400 rpm with a 10 : 1 BPR ratio. The as-prepared doped Cu–$BiVO_4$ samples were annealed at 450 °C for 2 hours under air atmosphere to improve the crystallinity. In the forthcoming sections, the prepared samples were referred to as A, B, C and D for undoped $BiVO_4$ and 1 at.%, 5 at.% and 10 at.% of copper in Cu–$BiVO_4$, respectively.

Characterization techniques

XRD patterns were recorded by using a PANalytical powder diffractometer with Cu Kα radiation (λ = 0.15418 nm) under an accelerating voltage of 30 kV and an emission current of 20 mA. The used scale of 2θ angle ranged from 18 to 52°. The optical properties were investigated by UV-Vis diffused reflectance method by using a Varian Cary 500 UV-Vis-NIR spectrometer in a wavelength range from 350 nm to 800 nm. Raman spectra were obtained using a Horiba Jobin Yvon Lab Ram-HR 800 Raman micro-spectrometer with an excitation line of He–Ne laser at 632.18 nm. The surface morphology and chemical compositions were characterized by FE-SEM, Carl Zeiss Auriga 60 (high vacuum, spot size 7.5 μm, 10 kV accelerating voltage) coupled with an energy-dispersive X-ray spectroscope (Bruker, PB-ZAF method, Sensor 5010, 129 eV resolution). HR-TEM observations were carried out using a JEOL ARM200F instrument operated at 200 kV accelerating voltage. EPR spectra were recorded in X-band (9.4 GHz) at a temperature of 150 K by using a Bruker EMX spectrometer with a cryogenic cryostat from Oxford Instruments. The resonance positions of EPR lines were accurately evaluated by using a characteristic EPR line of the dry DPPH sample associated with a *g*-factor of 2.0036. XPS was used to determine binding energies (BEs) related to molecular bonds of Bi, V, O and Cu involved at the surface of the Cu–$BiVO_4$ particles. The spectra were recorded using an XPS, PHI 5700 system with an Omni Focus IV lens system (Physical Electronics Inc.) with a monochromatic Al Kα X-ray source with the C1s signal at 284.6 eV used as a reference for BE calibration.

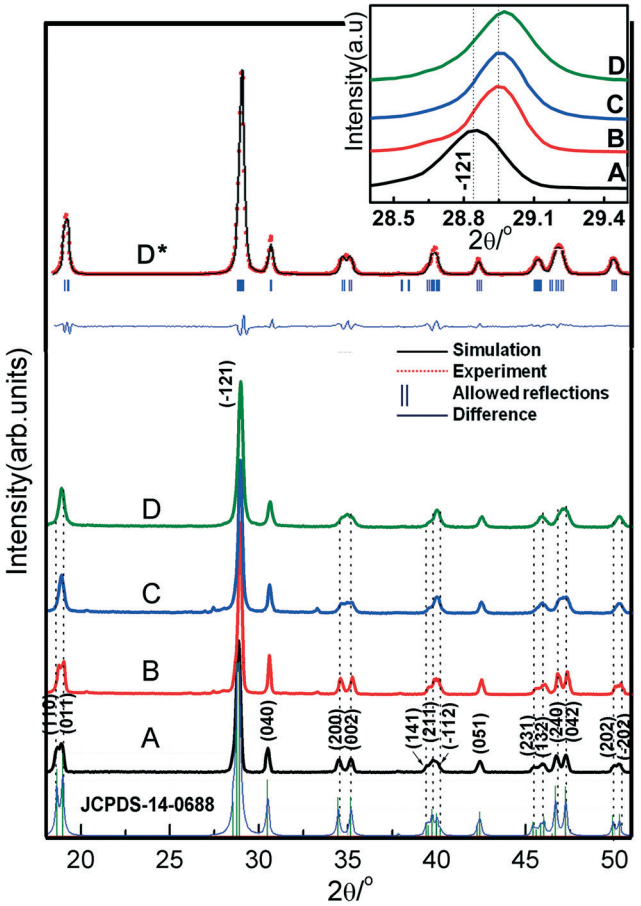

Fig. 2 X-ray diffraction patterns of copper-doped $BiVO_4$ nanopowders with different Cu doping ratios. The bottom pattern represents the reference diffraction pattern for monoclinic scheelite $BiVO_4$ referred to as JCPDS-14-0688. Samples labelled as A, B, C and D correspond to undoped $BiVO_4$ and 1 at.%, 5 at.% and 10 at.% Cu–$BiVO_4$, respectively. *D** represents FULLPROF refinement for 10 at.% Cu–$BiVO_4$. The inset shows the shift of 2θ towards a higher angle for a characteristic peak corresponding to the (−121) plane.

Results and discussion

Structural features from XRD studies

Diffraction patterns of Cu–$BiVO_4$ nanoparticles at different Cu concentrations exhibit a monoclinic scheelite phase according to the standard JCPDS data (014-0688) depicted in Fig. 2 along with a Cu–$BiVO_4$ refined pattern. It has been noticed that the high intense diffraction peak (−121) corresponding to the Cu–$BiVO_4$ samples shifts towards a higher angle (2θ) compared to pure $BiVO_4$ as shown in the inset of Fig. 2. This shift occurs from structural distortions such as compressive strains due to the incorporation of copper into the crystal sites of the $BiVO_4$ structure. The diffraction angle lines *N* {denoted by $N = h^2 + k^2 + l^2$} such as 2 (110, 011), 4 (200, 002), 6 (211, −112), 14 (231, 132), and 20 (240, 042) doublet peaks merged for highly doped Cu–$BiVO_4$ samples. The intensity of the lines depends on the arrangement of atoms in the unit cell. The decrease in the intensity and the increase in the FWHM of the diffraction lines can be induced by a disorder in the location of Cu inside the lattice or by distortions due to size differences between substituted ions. It is worth noting that all the as-prepared samples were annealed at the same temperature, *i.e.* 450 °C, which is defined from the best improvement of the crystal structure for the undoped sample. However, this temperature cannot be optimized to reproduce the good crystalline structure in heavily Cu-doped $BiVO_4$.

Crystal domain sizes of $BiVO_4$ and Cu–$BiVO_4$ were calculated from Scherrer's formula and reported in Table 1. The calculations consider the XRD line broadening FWHM values subtracted from the standard FWHM of the used reference LaB_6 fixed at $\Delta(2\theta) = 0.046°$. The average size of the crystalline domains in Cu–$BiVO_4$ is situated in the range of 33–40 nm with the lowest size in the heavily doped sample. The disorder of the copper ion distribution in the lattice and the shift of the annealing temperature required for improved

Table 1 Calculated coherent diffracting domains from Scherrer's formula and optical band gap values of the Cu–$BiVO_4$ samples

Samples	FWHM	2θ Position (−121)	Crystallite size (nm)	Band gap E_g (eV)
$BiVO_4$	0.220	28.86	37.78	2.41
1 at.% Cu–$BiVO_4$	0.206	28.946	40.49	2.40
5 at.% Cu–$BiVO_4$	0.231	28.958	35.9	2.37
10 at.% Cu–$BiVO_4$	0.2505	28.973	33.03	2.34

crystalline structure are plausibly the reason for the increased FWHM diffraction lines with the doping rates.

The doping process alters the crystallographic lattice parameters as illustrated below for the 10 at.% doped sample. Indeed, crystal unit cell dimensions were refined by the Rietveld method using the MAUD software. The diffraction patterns for doped and undoped samples were adjusted to the standard monoclinic system with space group $I2/c$. The refined data such as lattice parameters and characteristic 2θ shifts are summarized in Table 2 and depicted in Fig. 3 for various Cu doping rates. The refined crystallographic data reveal a reduction in lattice parameters with the amount of Cu-doping. The atomic positions of Bi, V, O1 and O2 summarized in Table 3 indicate lattice compression in the direction of crystallographic axes a and c and also suggest a compression in V–O covalent bonds of the VO_4 tetrahedron.[9] However, no drastic change seems to alter the weak molecular bonds of Bi–O, involved in dodecahedron arrangements. Since the calculated atomic radius of Cu (1.45 Å) is less than V (1.71 Å), the incorporation of Cu ions in the $BiVO_4$ matrix as substitution to V ions leads to a reduction in the lattice parameters.[19] Structural distortions in the VO_4 tetrahedron are expected to induce an internal electric field that contributes to the separation of electron–hole pairs. This is of particular interest for the photocatalytic processes as expected from metal-doped $BiVO_4$ materials.[9]

Raman investigations of vibrational features

Raman scattering spectroscopy is an efficient tool for probing the structure and bonding in metal-oxide species through their vibrational characteristics. In the monoclinic phase of $BiVO_4$, the Raman spectra (Fig. 4) exhibit six noticeable vibrational bands at 210, 327, 367, 637, 702 and 826 cm^{-1} which are related to the vibrational features of the VO_4 tetrahedron.[20] The intense band at 826 cm^{-1} was attributed to the shorter symmetric V–O stretching mode (A_g) and the weak bands at 702 and 637 cm^{-1} were assigned to the long (A_g) and short (B_g) asymmetric V–O stretching modes, respectively. The asymmetric and symmetric bending vibrations of the VO_4 tetrahedron were detected at 327 and 367 cm^{-1}, respectively, according to the assignment reported elsewhere.[21]

By using higher doping rates as 5 at.% and 10 at.%, the V–O stretching modes (819, 821 cm^{-1}) of the Cu–$BiVO_4$ are shifted to a lower wavenumber as compared to the pure sample or for a low doping rate (*i.e.* 1 at.%). Such results are consistent with elongation of bond length of V–O for highly Cu-doped $BiVO_4$ samples. Similar effects were reported in $BiVO_4$ grown by wet chemistry under different conditions where the shift of Raman bands is attributed to structural distortions which are induced by modified electronic band structures of $BiVO_4$.[22] In addition to the behaviour of the Raman band intensities, the FWHM of the major Raman band associated with symmetric stretching mode at 826 cm^{-1} expands with Cu content as illustrated in Fig. 8. This behaviour correlates with the degree of crystallinity or defects including oxygen vacancies. Similar effects were reported previously with other doping element as cobalt leading to shifts and overlap of the Raman bands of VO_4 tetrahedra.[23] The analysis of the Raman spectra corroborates the conclusions inferred from XRD investigations and gives consistent support to the structural evolution induced by Cu-doping in the monoclinic scheelite phase of $BiVO_4$.

Particle morphology and structure probed by FE-SEM and HR-TEM

FE-SEM microscopy images of Cu–$BiVO_4$ nanoparticles show a spherical shape and sizes ranging from 40 to 160 nm (Fig. 5). The particles are found to be composed of small and nanosized grains. The ImageJ 1.48v software was used for the quantitative evaluation of the particle size distribution. Noticeable reduction in the particle sizes was clearly seen for higher Cu-doped samples as traduced by particle size distribution plots reported in the inset. The main reason lies in the effect of Cu incorporation on the thermodynamic properties of the ball-milled powders as previously attributed to the fact that Cu-doping of $BiVO_4$ inhibits the particle growth.[24] The elemental composition analysis was performed by EDAX for Cu–$BiVO_4$ nanoparticles and their atomic (at.)% values are summarized in Table 4. Chemical element distribution

Table 2 Phase composition and crystallographic lattice parameters of monoclinic Cu-doped $BiVO_4$ nanopowders, refined by the Rietveld method from X-ray powder diffraction patterns

	Phase fraction				Crystal lattice parameters			
Sample name	$BiVO_4$	Bi_2O_3	V_2O_5	Crystal size (nm)	a (Å)	b (Å)	c (Å)	γ (°)
1 at.% Cu–$BiVO_4$	98.6 (±0.02)	1.3 (±0.008)	0 (±0)	43	5.189 (±3.2 e^{-4})	5.100 (3.2 e^{-4})	11.707 (6.4 e^{-4})	90.297
5 at.% Cu–$BiVO_4$	97.6 (±0.02)	2.3 (±0.004)	0 (±0)	40	5.161 (±4.2 e^{-4})	5.097 (4.1 e^{-4})	11.675 (8.4 e^{-4})	90.1806
10 at.% Cu–$BiVO_4$	100 (±0.03)	0 (±0)	0 (±0)	31	5.156 (±4.5 e^{-4})	5.097 (4.3 e^{-4})	11.607 (9.1 e^{-4})	90.1406

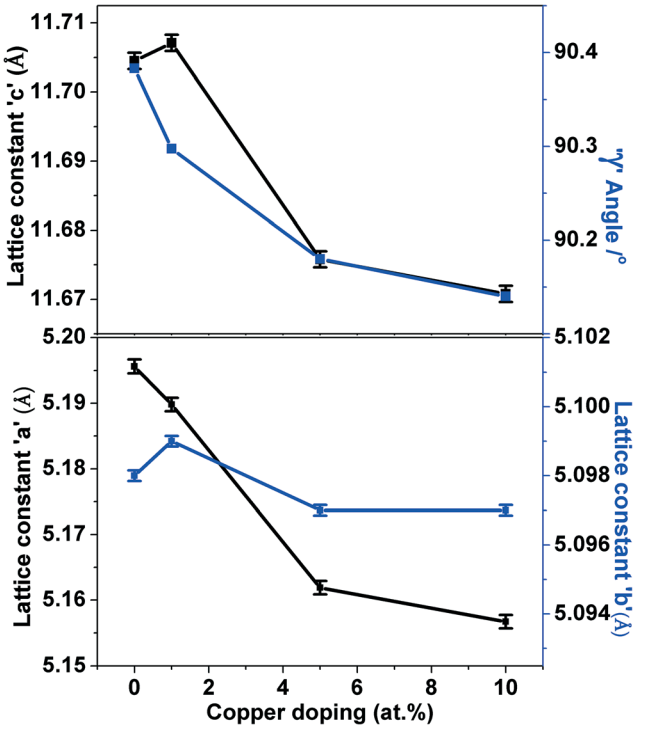

Fig. 3 Crystallographic lattice parameters obtained from refined XRD patterns by the Rietveld method for Cu–$BiVO_4$ samples.

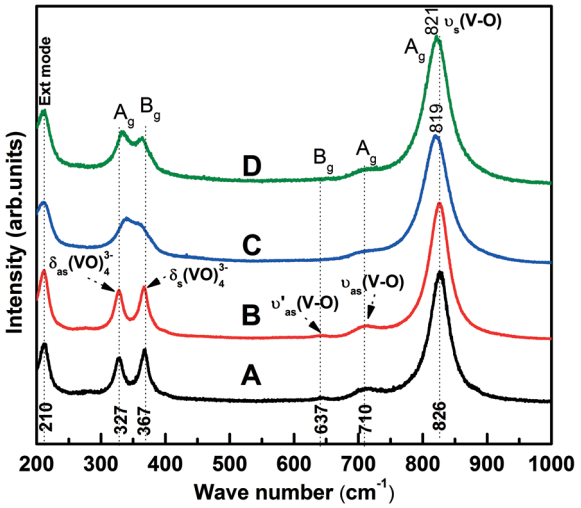

Fig. 4 Raman spectra of copper-doped $BiVO_4$ samples with the assignment of stretching and bending modes with their respective notations. Samples are referred to as A, B, C and D for undoped $BiVO_4$ and 1 at.%, 5 at.% and 10 at.% Cu–$BiVO_4$, respectively.

mappings were also carried out for Bi, O, V and doping ions Cu as illustrated in Fig. 5. Within the uncertainty of the EDAX, homogenous distributions of elements were inferred, testifying the absence of agglomeration or some phase segregations.

HR-TEM analysis of Cu–$BiVO_4$ particles reveals well crystalline domains (Fig. 6B, inset) through the resolved crystal lattice fringes for the considered samples (A, B, C, and D) with corresponding FFT crystallographic planes (Fig. 6). The inter-reticular distances d_{hkl}, in the crystalline monoclinic phase, were calculated for all the samples and the obtained values are associated with d_{110} = 0.474 nm, d_{011} = 0.467 nm, d_{040} = 0.312 nm and d_{220} = 0.237 nm. Although distortions of the lattice parameters were demonstrated with increased rates of Cu-doping, HR-TEM observations show good crystalline quality of doped samples.

Chemical bonding inferred from XPS investigations

As far as the chemical bonding with Cu ions is concerned, XPS analysis is a method of choice to probe the molecular bonding. XPS patterns were recorded on representative samples of Cu–$BiVO_4$. As shown in Fig. 7, XPS spectra reveal the binding energy levels of Bi 4f, V 2p, O 1s and Cu 2p. The binding energies of Cu species taking into account the spin orbital splitting of the 2p core level were found at E_b = 933 eV and 953 eV associated with the spectroscopic terms Cu-$2p_{1/2}$ and Cu-$2p_{3/2}$ doublet peaks, respectively, as illustrated in Fig. 7b. As can be seen from the XPS curves, the Cu–$BiVO_4$ sample possesses binding energies suggesting the presence of copper in oxidized form such as CuO or Cu_2O. In Fig. 7c, the XPS spectra related to Bi-4f consist of two intense and symmetrical peaks at E_b = 159.8 and 165.1 eV, corresponding to the Bi-$4f_{7/2}$ and Bi-$4f_{5/2}$ terms, respectively, in accordance with Bi ions in their trivalent oxidation state. The XPS spectrum of V $2p_{3/2}$ depicted in Fig. 7d can be deconvoluted into two peaks with energies E_b = 515.5 and 516.4 eV attributed to the surface V^{4+} and V^{5+} species, respectively. As a matter of fact, the stable oxidation state V^{5+} can be converted to V^{4+} due to surface effect (nanoparticles) or when oxygen vacancies are involved.[4]

For oxygen, O1s XPS spectra in Cu–$BiVO_4$ samples are shown in Fig. 7(e). The asymmetric peak centred at 530 eV was deconvoluted into two components. Different bonding states of the oxygen content coexist and are associated with binding energies E_b = 529.4 and 531.2 eV. Such values are assigned to lattice oxygen (O_{latt}) and adsorbed oxygen (O_{ads})

Table 3 Atomic positions of the monoclinic phase in Cu-doped $BiVO_4$ nanopowders refined by the Rietveld method

Sample name	Bi			V			O1			O2		
1 at.% Cu–$BiVO_4$	0 (±0.002–0.003)	0.249	0.632	0 (±0.002–0.003)	0.25	0.128	0.144 (±0.002–0.003)	0.472	0.2019	0.325 (±0.002–0.003)	0.353	0.429
5 at.% Cu–$BiVO_4$	$4.7\ e^{-4}$ (±0.002–0.003)	0.25	0.63	0.01 (±0.002–0.003)	0.315	0.111	0.137 (±0.002–0.003)	0.55	0.22	0.278 (±0.002–0.003)	0.384	0.428
10 at.% Cu–$BiVO_4$	$2.5\ e^{-4}$ (±0.002–0.003)	0.249	0.635	0.012 (±0.002–0.003)	0.31	0.116	0.132 (±0.002–0.003)	0.55	0.216	0.28 (±0.002–0.003)	0.383	0.435

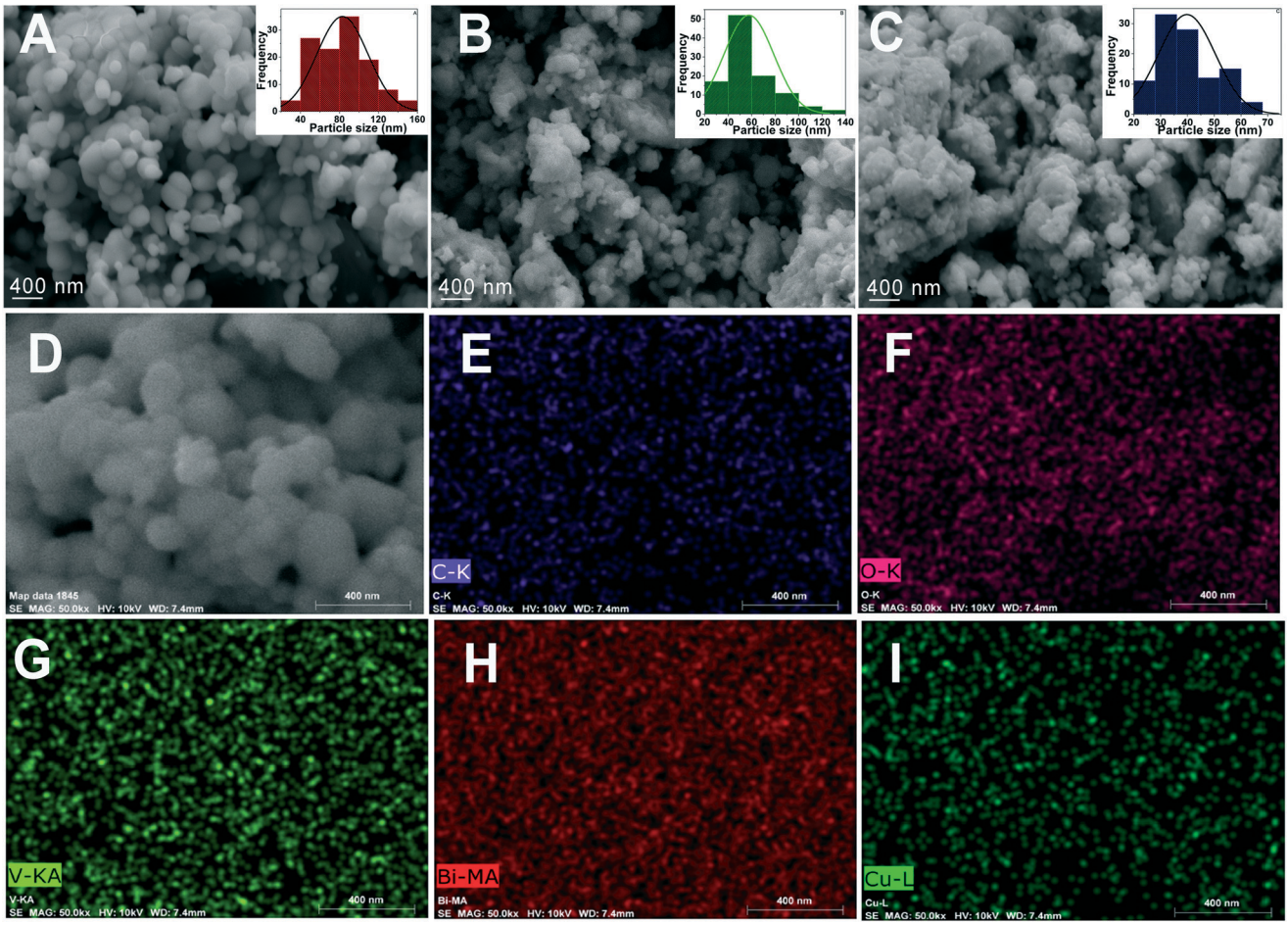

Fig. 5 FE-SEM images of copper-doped $BiVO_4$ nanopowders for (A) 1 at.%, (B) 5 at.%, and (C) 10 at.%. The inset shows the particle size distribution. Elemental mapping from EDAX composition profile for 5 at.% in the Cu–$BiVO_4$ sample (D). (E) Carbon k-line from the substrate, (F) oxygen k-line, (G) vanadium k-alpha line, (H) bismuth m-alpha line and (I) copper l-line.

species, respectively.[25] However, the O_{ads}/O_{latt} molar ratios are relatively high for all the samples irrespective to the powder morphologies and the doping rates. XPS results which are more sensitive to surface compositions are completed, as discussed below, by EPR experiments which probe precisely the Cu^{2+} and V^{4+} ions for their absolute concentrations as well as their local environments in the samples.

EPR studies of Cu-doped $BiVO_4$

EPR spectroscopy is a sensitive tool to probe the doping process or surface effects where the oxidation state of a particular ion leads to electronic configurations with unpaired spins.

Table 4 Energy dispersive X-ray spectroscopy showing the chemical compositions of the Cu–$BiVO_4$ samples

Cu (at.%) experimental	Bismuth (at.%)	Vanadium (at.%)	Oxygen (at.%)	Cu (at.%) (EDAX)
0	16.46	17.54	66.0	—
1	15.36	15.66	67.99	0.99
5	18.88	19.36	59.94	1.82
10	19.09	18.87	59.28	2.76

The situation of the monoclinic $BiVO_4$ structure doped by copper ions is worthy of interest. Indeed, in a perfect crystalline structure, vanadium ions possess the valence state V^{5+} state leading to spinless ions. However, due to oxygen vacancies induced notably in nanosized particles with high specific surfaces, the departure of vanadium to its normal valence state leads to reduced species as V^{4+} which are paramagnetic ions. The electronic configuration of V^{4+} ($3d^1$) possesses an effective electronic spin ($S = 1/2$) giving rise to an EPR signal. For copper doping of $BiVO_4$, the oxygen environment stabilizes the oxidation state Cu^{2+} with an electronic configuration ($3d^9$) giving rise to an EPR signal with an electronic spin $S = 1/2$. The EPR spectra of Cu–$BiVO_4$ are summarized in Fig. 8A for different doping ratios. Each EPR spectrum is composed of two contributions traduced by a central isotropic sharp EPR line superimposed to a broad and structured resonance band. The experimental EPR spectra were adjusted by using the Bruker-Winsinfonia software. Thus, the single EPR line is associated with V^{4+} ($3d^1$) with regard to the magnetic interaction marked by an isotropic g-Landé tensor with diagonal components $g_x = g_y = g_z = 1.97$. The EPR signal associated with Cu^{2+} ions is accounted by an anisotropic magnetic

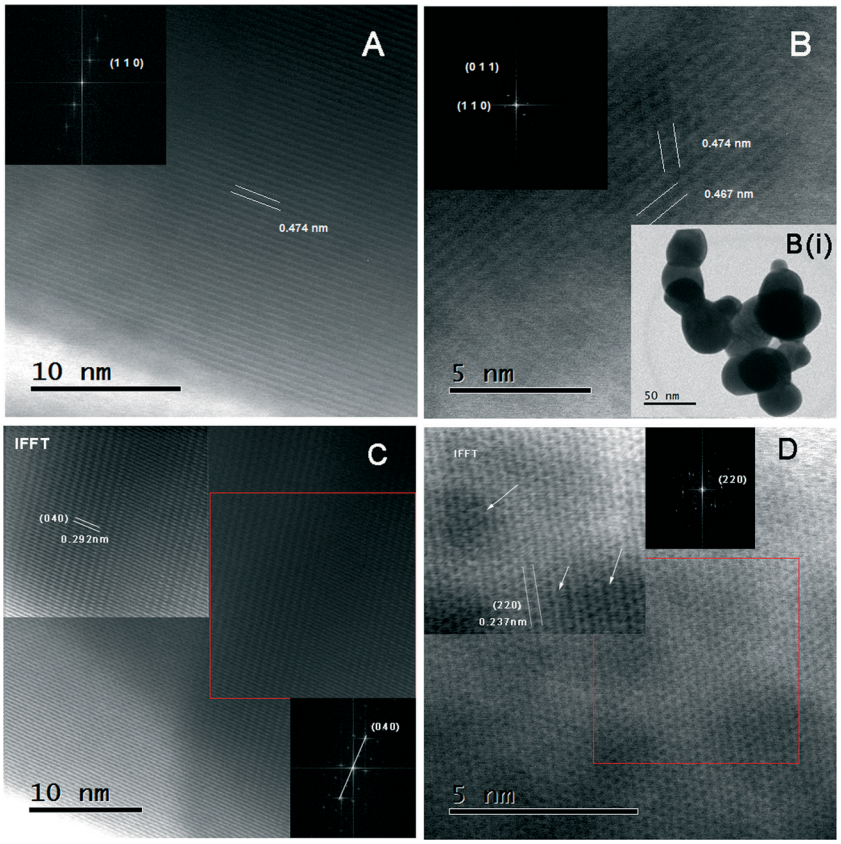

Fig. 6 HR-TEM images with the corresponding FFT shown in the inset for Cu–$BiVO_4$ samples. (A) Undoped, (B) 1 at.% with inset (i) showing a particle size of around 50 nm, (C) 5 at.% with the inset showing an IFFT image and (D) 10 at.% with the inset showing an IFFT image of a distorted lattice indicated by arrows.

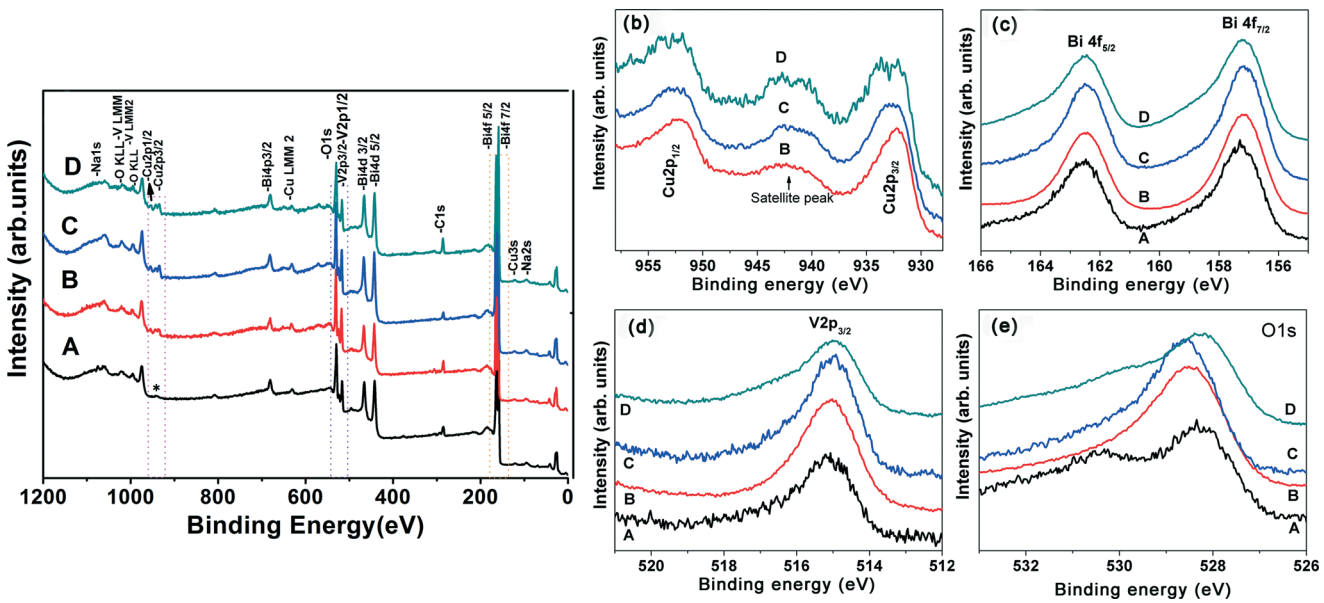

Fig. 7 XPS spectra for undoped and Cu-doped $BiVO_4$ samples, where A, B, C and D are associated with undoped $BiVO_4$ and 1 at.%, 5 at.% and 10 at.% Cu–$BiVO_4$, respectively; (b, c, d and e) the binding energies of Cu 2p, Bi 4f, O 1s and V 2p orbitals.

Landé tensor $g_x = 2.15$, $g_y = 2.07$ and $g_z = 2.35$. The Cu^{2+} EPR line width (100–200 Gauss) and also V^{4+} (100 Gauss) as well as the unresolved hyperfine structures for both ions are accounted by dipolar or exchange interactions between

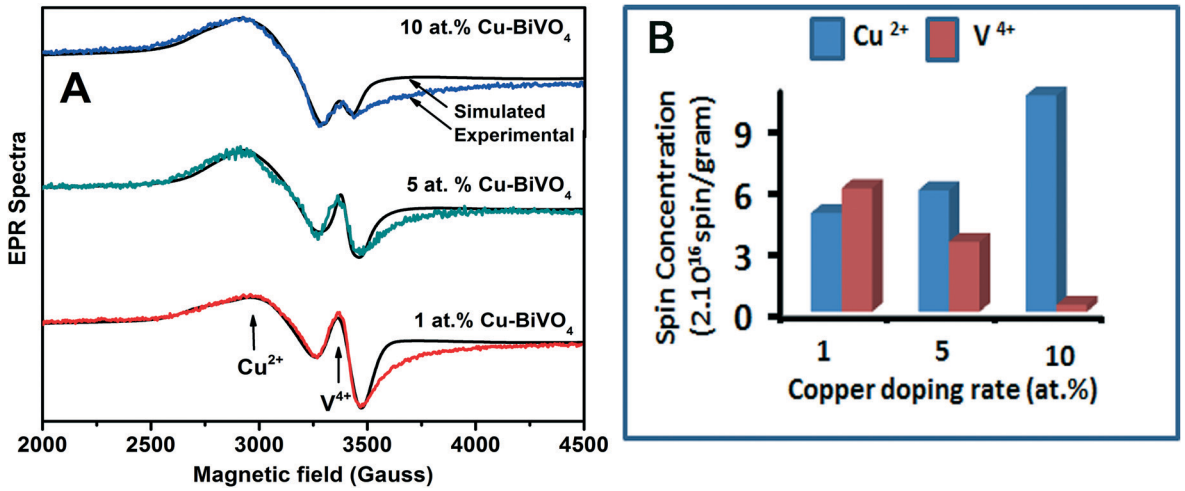

Fig. 8 (A) EPR spectra of copper-doped $BiVO_4$ samples with different copper doping rates. (B) Absolute concentrations of Cu^{2+} and V^{4+} ions and their evolution with copper doping rate.

copper and vanadium ions situated at relatively short distances. In other words, this effect traduces the possibility of agglomerated paramagnetic species. On the other hand, the rate V^{4+}/V^{5+} is more important for low copper doping rates and drastically decreases with increased copper concentrations in the samples. Meanwhile, the evolution of the EPR spectrum intensity related to copper ions did not follow the initial doping rate. Such behaviour is plausibly due to the occurrence of efficient charge transfer between Cu^{2+} and V^{4+} as well as the suppression of oxygen vacancies which contributes to the creation of reduced vanadium. Quantitatively, the absolute concentrations of these ions were obtained from the double integration of the EPR spectra related to each paramagnetic ion and using a reference sample ($CuSO_4$) with calibrated spin concentration. The results summarized in Fig. 8B give a quantitative evaluation of Cu^{2+} content in the investigated samples as well as active electronic centres as V^{4+}. Concentrations of Cu^{2+} were found to increase with the doping rate from 0.8×10^{17} (initial doping 1 at.%) up to 2×10^{17} ions per gram (initial 10 at.%). For vanadium ions V^{4+}, a decrease in its concentration from 1.2×10^{17} down to 0.3×10^{16} spins per gram occurs with an increase in doping from 1 at.% to 10 at.%.

To sum up, the EPR experiments show the existence of reduced valence states of vanadium ions (V^{4+}) along with oxidized environments of copper ions (Cu^{2+}). The effective concentration of Cu^{2+} in the samples is evaluated with good accuracy. Dipolar or exchange interactions are involved between copper and vanadium ions as well as charge transfer between these species. This process contribute to the photocatalytic activity of Cu–$BiVO_4$ materials as shown in the ESI† associated with this article (Fig. S1).

UV-visible optical absorption of $BiVO_4$ powders

The optical absorption spectrum of a semiconducting material is monitored by its electronic structure which defines the threshold and the concerned spectral range. The doping process is dedicated to extend the optical absorption on a larger visible range leading to visible light-driven photocatalysis. In the case of undoped $BiVO_4$, the main absorption band is expanded on the wavelength range of 350–530 nm. In doped Cu–$BiVO_4$ powders, broad shoulder and extended absorption background appear on the main band over the range of 530–800 nm and their importance correlates with the Cu content as depicted in Fig. 9a. By using the Tauc plot based on the absorbance and incident photon energy $h\nu$, the following relation (eqn (1)) serves to evaluate the direct band gap value:

$$\alpha \cdot h\nu = A(h\nu - E_g)^{n/2} \quad (1)$$

α, A, n and E_g represent the absorption coefficient, a constant of proportionality, an index with different values (1, 3, 4, 6) depending on the nature of optical transition and the direct band gap energy, respectively. The threshold absorption edges were evaluated by an asymptotic extrapolation (Fig. 9b) for the pure sample and for Cu-doped $BiVO_4$ with doping rates of about 1, 5 and 10 at.%. The obtained values were, respectively, 2.41, 2.40, 2.37 and 2.34 eV for the "pseudo-direct" band gap of $BiVO_4$. The term "pseudo" is used due to a favourable direct transition between VB and CB which occurs outside the Brillouin zone center.[26] Indeed, the minimum of conduction band (CBM) is located at the Z point which corresponds to the (0.000, −0.500, 0.500) direction in the Brillouin zone. In addition to fundamental absorption threshold edges, broad shoulders are observed at 2.01 and 1.98 eV in the 5 and 10 at.% Cu-doped samples, respectively. The involved atomic orbitals in VB are composed of Bi (6 s) and O (2p), while they are composed of V (3d) states for CB. The optical band gap is then defined by transitions between VB and CB with finite probability at the Z point. In the doped samples, copper ions contribute, on the one hand, to lower the band gap by introducing allowed states within the band gap. On the other hand, the Cu–O environments

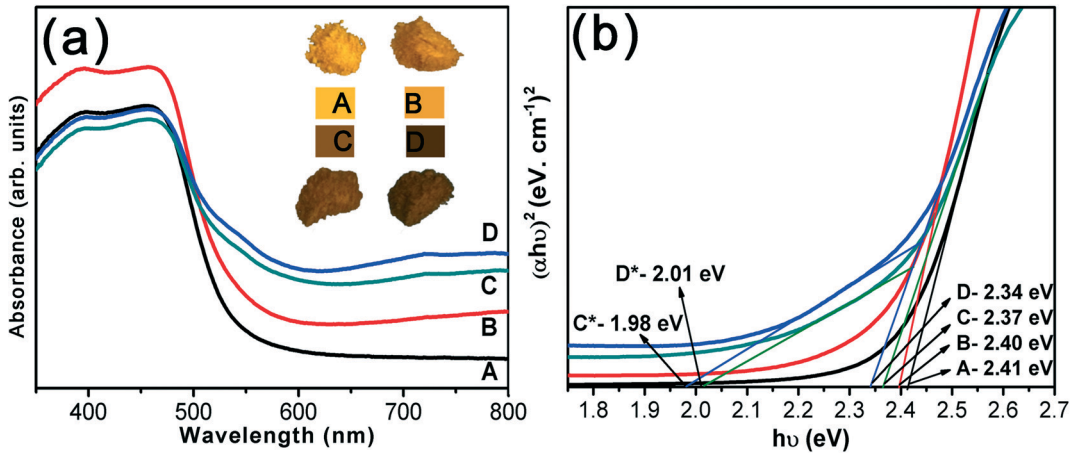

Fig. 9 (a) UV-Vis diffuse absorption spectra of $BiVO_4$ samples: (A) undoped $BiVO_4$, (B) 1 at.%, (C) 5 at.% and (D) 10 at.% Cu–$BiVO_4$, respectively. The inset in (a) shows the color of the Cu-doped $BiVO_4$ powders with different Cu concentrations. (b) The band gap energy values for Cu-doped $BiVO_4$ obtained from the Tauc plot.

demonstrated by EPR and XPS favour the occurrence of transitions between O (2p) and Cu (3d). The broad shoulder on the main absorption band can be accounted by the copper doping in agreement with a large effect with increasing doping rate. This effect correlates well with the colour of Cu-doped $BiVO_4$ samples, which changes from bright yellow (pure $BiVO_4$) to dark brown as shown in Fig. 9a (inset). The colour change is a feature of a semiconductor material, which is dependent on its electronic structure and considered as an important factor for photocatalytic activity.[27] The broad background absorption can be accounted by intermediate electronic levels induced in the band gap by Cu substitution in the host crystal sites. This effect enhances the photocatalytic efficiency compared to undoped materials as reported in the ESI† (Fig. S1).

Conclusion

Cu-doped $BiVO_4$ nanoparticles were synthesized by the mechano-chemical technique with improved processing parameters and post-synthesis treatments to optimize the crystal structure. Thus, a monoclinic scheelite structure was obtained for representative samples with different Cu doping ratios. XRD and micro-Raman investigations were analyzed by considering structural distortions with quantitative estimation of the lattice parameters and the lattice compression as function of the Cu doping rates. Spherical nanoparticles distributed in the range of 40–160 nm were estimated from FE-SEM images with the tendency to decrease their sizes for higher Cu-doped samples. XPS analysis determined the chemical bonding involved between the constitutive elements and including the Cu location in the host lattice. Mixed oxidation states of V^{4+}/V^{5+} with variable concentrations were shown from XPS spectra also supported by EPR experiments and correlate with the Cu doping ratios. The effective concentrations of copper ions in the valance state Cu^{2+} as well as that of the reduced form of vanadium ions V^{4+} were quantitatively determined by EPR. The features of the EPR spectra and the evolution of these concentrations with the copper doping rate indicate the occurrence of interactions and charge transfer between these electronic active species. These results suggest that the mechanism of charge transfer required for photocatalysis reactions would be affected by Cu doping. Finally, UV-Vis optical absorption bands show an extension in the spectral range of 530–800 nm by Cu doping. This evolution of optical features is of particular interest for visible light-driven photocatalysis based on a stabilized scheelite monoclinic structure in Cu–$BiVO_4$.

Acknowledgements

V. I. Merupo gratefully acknowledges the financial support given by CONACYT – Becas mixtas, Mexico and Doctoral School 3MPL – University of Maine, Le Mans, France. K. Ordon has benefited from the financial support of Polonium program 31 300 TA provided by the French Embassy in Warsaw. The authors would like to thank Prof. Alain Bulou for micro-Raman spectrometry measurements and Alvaro Angeles from LANE CINVESTAV-IPN for HR-TEM characterization. We also acknowledge the financial support extended from the project between CINVESTAV and the University of Maine through their joint funds.

References

1 (*a*) M. H. Alonso, F. Fresno, S. Suarez and J. M. Coronado, *Energy Environ. Sci.*, 2009, **2**, 1231–1257; (*b*) M. R. Hoffmann, S. T. Martin, W. Choi and D. W. Bahnemannt, *Chem. Rev.*, 1995, **95**(1), 69–96; (*c*) Q. Xiang, J. Yu and M. Jaroniec, *Chem. Soc. Rev.*, 2012, **41**, 782–796; (*d*) A. O. Ibhadon and P. Fitzpatrick, *Catalysts*, 2013, **3**(1), 189–218; (*e*) H. Xu, S. Ouyang, L. Liu, P. Reunchan, N. Umezawaace and J. Ye, *J. Mater. Chem. A*, 2014, **2**, 12642–12661.

2 (*a*) X. Chen and S. S. Mao, *Chem. Rev.*, 2007, **107**, 2891–2959; (*b*) W. Doerffler and K. Hauffe, *J. Catal.*, 1964, **3**, 171–178; (*c*) F. Steinbach, *Nature*, 1969, **221**, 657–658; (*d*) T. K.

Townsend, N. D. Browning and F. E. Osterloh, *ACS Nano*, 2012, **6**(8), 7420–7426; (*e*) A. A. Ashkarran, A. I. Zad, M. M. Ahadian and S. A. M. Ardakani, *Nanotechnology*, 2008, **19**, 195709 (7 pp.).

3 D. L. Liao and B. Q. Liao, *J. Photochem. Photobiol., A*, 2007, **187**, 363.

4 (*a*) R. Venkatesan, S. Velumani and A. Kassiba, *Mater. Chem. Phys.*, 2012, **135**(2, 3), 842–848; (*b*) R. Venkatesan, S. Velumani, M. Tabellout, N. Errien and A. Kassiba, *J. Phys. Chem. Solids*, 2013, **74**(12), 1695–1702.

5 (*a*) Y. T. Ho, C. S. Ho, S. K. Jeong and J. M. Su, *J. Phys.: Condens. Matter*, 1994, **6**, 383–392; (*b*) I. C. Vinke, J. Diepgrond, B. A. Boukamp, K. J. de Vries and A. J. Burggraaf, *Solid State Ionics*, 1992, **57**, 83–89.

6 (*a*) J. Su, L. Guo, N. Bao and C. A. Grimes, *Nano Lett.*, 2011, **11**, 1928–1933; (*b*) H. Jiang, H. Endo, H. Natori, M. Nagai and K. Kobayashi, *Mater. Res. Bull.*, 2009, **44**, 700–706.

7 A. Walsh, Y. Yan, M. N. Huda, M. M. Al-Jassim and S. Wei, *Chem. Mater.*, 2009, **21**, 547–551.

8 (*a*) S. Tokunaga, H. Kato and A. Kudo, *Chem. Mater.*, 2001, **13**(12), 4624–4628; (*b*) X. Zhang, Z. Ai, F. Jia, L. Zhang, X. Fan and Z. Zou, *Mater. Chem. Phys.*, 2007, **103**, 162–167.

9 (*a*) Z. Zhao, Z. Li and Z. Zou, *Phys. Chem. Chem. Phys.*, 2011, **13**, 4746–4753; (*b*) H. S. Park, K. E. Kweon, H. Ye, E. Paek, G. S. Hwang and A. J. Bard, *J. Phys. Chem. C*, 2011, **115**, 17870–17879.

10 (*a*) H. Fan, D. Wang, L. Wang, H. Li, P. Wang, T. Jiang and T. Xie, *Appl. Surf. Sci.*, 2011, **257**, 7758–7762; (*b*) H. Li, G. Liu, S. Chen, Q. Liu and W. Lu, *Phys. E*, 2011, **43**, 1323; (*c*) J. Su, L. Guo, S. Yoriya and C. A. Grimes, *Cryst. Growth Des.*, 2010, **10**(2), 856–861.

11 M. Yao, M. Liu, L. Gan, F. Zhao, X. Fan, D. Zhu, Z. Xu, Z. Hao and L. Chen, *Colloids Surf., A*, 2013, **433**, 132–138.

12 M. Wang, H. Zheng, Q. Liu, C. Niu, Y. Che and M. Dang, *Spectrochim. Acta, Part A*, 2013, **114**, 74–84.

13 H. Xu, H. Li, C. Wu, J. Chu, Y. Yan and H. Shu, *Mater. Sci. Eng., B*, 2008, **147**, 52–56.

14 H. Jiang, H. Dai, X. Meng, L. Zhang, J. Deng, Y. Liu and C. T. Au, *J. Environ. Sci.*, 2012, **24**(3), 449–457.

15 S. Kohtani, J. Hiro, N. Yamamoto, A. Kudo, K. Tokumura and R. Nakagaki, *Catal. Commun.*, 2005, **6**, 185–189.

16 H. Q. Jiang, H. Endo, H. Natori, M. Nagai and K. Kobayashi, *J. Eur. Ceram. Soc.*, 2008, **28**, 2955–2962.

17 A. Kudo, K. Ueda, H. Kato and I. Mikami, *Catal. Lett.*, 1998, **53**, 229–230.

18 M. Long, W. M. Cai and H. Kisch, *J. Phys. Chem. C*, 2008, **112**, 548–554.

19 Y. Yang, Q. Zhang, B. Zhang, W. B. Mi, L. Chen, L. Li, C. Zhao, E. M. Diallo and X. X. Zhang, *Appl. Surf. Sci.*, 2012, **258**, 4532–4537.

20 L. S. Kumari, P. P. Rao, A. N. P. Radhakrishnan, V. James, S. Sameera and P. Koshy, *Sol. Energy Mater. Sol. Cells*, 2013, **112**, 134–143.

21 F. D. Hardcastle and I. E. Wachs, *J. Phys. Chem.*, 1991, **95**, 5031–5041.

22 (*a*) W. Ma, Z. Lu and M. Zhang, *Appl. Phys. A: Mater. Sci. Process.*, 1998, **66**, 621–627; (*b*) J. Yu and A. Kudo, *Adv. Funct. Mater.*, 2006, **16**, 2163–2169.

23 (*a*) J. Yu and A. Kudo, *Adv. Funct. Mater.*, 2006, **16**(16), 2163–2169; (*b*) A. P. Zhang, J. Z. Zhang, N. Y. Cui, X. Y. Tie, Y. W. An and L. J. Li, *J. Mol. Catal. A: Chem.*, 2009, **304**, 28–32.

24 M. Wang, Q. Liu, Y. Che and D. Zhang, *J. Alloys Compd.*, 2013, **548**, 70–76.

25 H. Y. Jiang, H. X. Dai, X. Meng, L. Zhang, J. G. Deng and K. M. Ji, *Cuihua Xuebao*, 2011, **32**(6), 939–949.

26 (*a*) A. Kudo, R. Niishiro, A. Iwase and H. Kato, *Chem. Phys.*, 2007, **339**(1–3), 104–110; (*b*) A. Walsh, Y. Yan, M. N. Huda, M. M. Al-Jassim and S. H. Wei, *Chem. Mater.*, 2009, **21**, 547–551.

27 A. P. Zhang and J. Z. Zhang, *Wuli Huaxue Xuebao*, 2010, **26**, 1337–1342.

